Journal of Computational Physics (2020)

Contents lists available at ScienceDirect

Journal of Computational Physics

journal homepage: www.elsevier.com/locate/jcp

A ghost structure finite difference method for a fractional FitzHugh-Nagumo monodomain model on moving irregular domain

Yongheng Wang[a], Li Cai[a,*], Xiaobing Feng[b,*], Xiaoyu Luo[c], Hao Gao[c]

[a]*NPU-UoG International Cooperative Lab for Computation and Application in Cardiology, School of Mathematics and Statistics, Northwestern Polytechnical University, Xi'an, 710129, China*
[b]*Department of Mathematics, The University of Tennessee, Knoxville, TN 37918, U.S.A.*
[c]*School of Mathematics and Statistics, University of Glasgow, Glasgow, G12 8QQ, UK*

ARTICLE INFO

Article history:
Received 1 May 2013
Received in final form 10 May 2013
Accepted 13 May 2013
Available online 15 May 2013

Communicated by S. Sarkar

ABSTRACT

In this paper, a ghost structure (GS) finite difference method is proposed to simulate the fractional FitzHugh-Nagumo (FHN) monodomain model on a moving irregular computational domain. In the GS formulation the moving irregular domain is converted into a fixed regular domain (called ghost structure), and the transmembrane potential is described in the Eulerian coordinates, while the membrane dynamics are described in the Lagrangian coordinates. The transformation between the Lagrangian variables and the Eulerian variables is achieved by an integral transformation which involves a delta function. The GS formulation allows to compute the transmembrane potential in a fixed regular domain using the finite difference method on a Cartesian grid, which has a huge advantage for approximating domain-dependent fractional derivatives. To overcome the difficulty caused by running time-consuming loops to compute the transformation between the Eulerian and Lagrangian variables, two fast algorithms are proposed to compute the transformation. Extensive numerical tests are provided to demonstrate the effectiveness and robustness of the proposed GS finite difference method for solving the fractional FHN monodomain model. We first numerically study the transmembrane potential propagation in both healthy hearts and hearts with arrhythmia by simulating the model in the transverse of a ventricle. We then study the transmembrane potential propagation during the pumping process, which requires to simulate the model in the moving longitudinal section of a ventricle. Our numerical results show that the change of spatial derivatives can affect the propagation velocity and the width of the transmembrane potential wave, and for a heart with arrhythmia, the transmembrane potential begins to enter cyclically the region where cardiomyocytes have been excited and then stimulates cardiomyocytes to contract again.

1. Introduction

A heart can be thought of as a rhythmic pump that maintains blood circulation throughout the body[1]. The rhythmic beating of the heart is the result of the regular spread of action potential (AP) in the heart. Abnormal conduction of AP in the heart can cause arrhythmias. Sudden cardiac death accounts for 15% of global fatalities, and about 80% of sudden cardiac deaths is caused by ventricular arrhythmias [2]. Thus, studying and understanding the mechanism of arrhythmia becomes crucial for preventing and curing cardiac deaths and diseases. Numerical simulations of electrical activity have become a powerful tool for understanding and studying the mechanism of arrhythmia and cardiac electrophysiology [3, 4, 5], because numerical simulations can be done to examine extreme situations that are difficult and/or expensive to achieve by experiments.

As the cardiac tissue is composed of cardiomyocytes, consequently, the electrophysiological modeling of cardiomyocytes is the most basic study of heart research, in which the excitatory diffusion in the cardiomyocytes is often sought-after. The best known such a model is the widely used unicellular monodomain electrophysiological model proposed by FitzHugh and Nagumo [6] which has been used to describe the potential propagation in heterogeneous heart tissues [7, 8]. The spatial complexity of a medium is expected to alter the laws of standard diffusion [9, 10], but it is still unclear to what extent the electrical propagation is influenced by the heterogeneity of the heart tissue [11]. Most heart models treat the tissue as continuum media with spatially averaged properties and neglect the contribution of its microstructure in modulating electrical conduction. While many mechanical characteristics have been obtained by using those traditional models, their limitations in characterizing tissue structures have already been noticed [12]. Improved models must be developed in order to overcome these limitations. One idea is to replace the classical FitzHugh and Nagumo (FHN) model by a fractional FHN model (see Section 2) to describe the complex material properties of cardiomyocytes and to simulate the AP propagation in a heart. Indeed, Feng et al. [13] and Yang et al. [14] developed some finite element methods for the fractional FHN model, and the latter work focused on solving the involved nonlinear reaction-diffusion equation in irregular domains. Liu et al. [15] proposed a new fractional finite volume method for fractional diffusion equations and applied it to the fractional FHN model. Cai et al. [16] developed a modified nonstandard finite difference method for the two-dimensional Riesz space fractional reaction-diffusion equations, and established the stability and convergence for the proposed scheme. It should be noted that all these works only considered the fractional models in a fixed domain, their results do not apply when the physical domain varies in time (called a moving domain), which is the case for heart simulation.

We also note that fractional calculus and fractional differential models have gained a lot attention and popularity in the past fifteen years (cf. [17] and the references therein). Compared with the integer-order differential equations, fractional differential equations can more effectively describe the memory effect, heredity, and non-locality involved in complex environments [17, 18]. As a result, they have been widely used in many scientific fields, such as bioengineering [19], pharmacokinetics [20], electrical conduction system [21], and image processing [22], just name a few. As in the integer-order case, most nonlinear fractional differential equations are not solvable by analytical methods, hence, numerical methods, including the finite difference method [23, 24], the finite element method [25, 26], the spectral method [27] and the finite volume method [28], must be employed to solve them. In addition, high-order numerical methods were also developed for fractional differential equations. Jiang et al. [29] introduced high-order finite element methods for solving a class of time fractional partial differential equations, and established the optimal rate of convergence for the proposed method. Ren et al. [30] proposed a fourth-order compact scheme for solving the time fractional diffusion-wave equation with Neumann boundary conditions, and proved the unconditional stability and the global convergence of the compact difference scheme. However, all these existing methods only can solve the fractional differential equations in regular rectangular domains, they could not be easily extended irregular and moving domains, because the definitions of fractional derivatives are strongly domain-dependent and dimension-dependent.

The goal of this paper is to develop a ghost structure (GS) finite difference method for solving the fractional FitzHugh-Nagumo (FHN) monodomain model on a moving irregular computational domain. In the GS formulation, the moving irregular domain is converted into a fixed regular domain (called ghost structure), and the transmembrane

*Corresponding author:
e-mail: caili@nwpu.edu.cn (Li Cai), xfeng@math.utk.edu (Xiaobing Feng)

potential is described in the Eulerian coordinates, while the membrane dynamics are described in the Lagrangian coordinates. The transformation between the Lagrangian variables and the Eulerian variables is achieved by an integral transformation which involves a delta function, fast algorithms ought be used to efficiently compute this transformation. The GS formulation allows to compute the transmembrane potential in the fixed regular ghost structure using the finite difference method on a Cartesian grid, which has a huge advantage for approximating domain-dependent fractional derivatives. The proposed GS finite difference method can simulate the fractional monodomain model in the moving deformed structure similar to the immersed boundary method [31, 32, 33] does for the fluid-solid coupling problems.

The remainder of this paper is organized as follows. In Section 2, we introduce the preliminaries and the fractional FHN monodomain model to be solved in this paper. In Section 3, we present the ghost structure formulation for the fractional FHN model. In Section 4, we first introduce our space and time finite difference discretization of the GS formulation, we then propose two fast algorithms for computing the integral transformation involving the delta function. In Section 5, we present several numerical experiments to verify the effectiveness and robustness of the proposed GS finite difference method and provide the numerical results of the transmembrane potential propagation in the stationary transverse section of a ventricle. In the meantime, in order to verify the effectiveness of the GS method for handling moving domains, we also provide a numerical test which simulates the transmembrane potential propagation in the moving longitudinal section of a ventricle. Finally, the paper is concluded with some concluding remarks and discussions given in Section 6.

2. The fractional FitzHugh-Nagumo monodomain model

Before introducing the fractional FitzHugh-Nagumo (FHN) monodomain, we first recall that the classical integer-order (dimensionless) FHN monodomain model has the following form (cf. [34, 35]):

$$\frac{\partial \widetilde{u}}{\partial t} = \nabla \cdot (\widetilde{\mathbf{K}} \nabla \widetilde{u}) + I_{\text{ion}}(\widetilde{u}, \widetilde{v}) \qquad \text{in } \Omega_s(t) \times (0, T), \tag{1a}$$

$$\frac{\partial \widetilde{v}}{\partial t} = g(\widetilde{u}, \widetilde{v}) \qquad \text{in } \Omega_s(t) \times (0, T), \tag{1b}$$

where $\widetilde{u}$ and $\widetilde{v}$ are two scalar-valued functions which denote, respectively, the Lagrangian transmembrane potential and recovery variable, I_{ion} is a known function of $\widetilde{u}$ and $\widetilde{v}$ which describes the ionic current through a number of different types of ion channels. $\widetilde{\mathbf{K}}$ denotes the Lagrangian diffusion coefficient. g is a nonlinear function of $\widetilde{u}$ and $\widetilde{v}$ that relates the ionic flux to the total ionic current. $\mathbf{X} = (X, Y) \in \Omega_s(0)$ stands for Lagrangian (material) coordinates. The mapping $\chi(\mathbf{X}, t) = (X_t, Y_t)$ provides the physical position of each Lagrangian point $\mathbf{X}$ at time t. Therefore, the physical region occupied by myocardium at time t is given by $\Omega_s(t) = \chi(\Omega_s(0), t)$, which is a moving domain. Figure 1 depicts such an example. The segments of the whole boundary $\Gamma_{\Omega_s}(t)$ of the moving domain $\Omega_s(t)$ can be described as follows:

$$\begin{aligned}
\widetilde{B}_a(Y_t) &= \min\{X_t : (X_t, \eta) \in \Omega_s(t), \eta = Y_t\},\\
\widetilde{B}_b(Y_t) &= \max\{X_t : (X_t, \eta) \in \Omega_s(t), \eta = Y_t\},\\
\widetilde{B}_c(X_t) &= \min\{Y_t : (\xi, Y_t) \in \Omega_s(t), \xi = X_t\},\\
\widetilde{B}_d(X_t) &= \max\{Y_t : (\xi, Y_t) \in \Omega_s(t), \xi = X_t\},
\end{aligned}$$

where $\widetilde{B}_a(Y_t)$ and $\widetilde{B}_b(Y_t)$ represent, respectively, the left and right portion of $\Gamma_{\Omega_s}(t)$, and $\widetilde{B}_c(X_t)$ and $\widetilde{B}_d(X_t)$ are the lower and upper portion of $\Gamma_{\Omega_s}(t)$.

The 2D fractional FHN monodomain model considered in this paper is given by

$$\frac{\partial \widetilde{u}}{\partial t} := \widetilde{K}_X \frac{\partial^\alpha \widetilde{u}}{\partial |X_t|^\alpha} + \widetilde{K}_Y \frac{\partial^\beta \widetilde{u}}{\partial |Y_t|^\beta} + I_{\text{ion}}(\widetilde{u}, \widetilde{v}) \qquad \text{in } \Omega_s(t) \times (0, T), \tag{2a}$$

$$\frac{\partial \widetilde{v}}{\partial t} := g(\widetilde{u}, \widetilde{v}) \qquad \text{in } \Omega_s(t) \times (0, T), \tag{2b}$$

Fig. 1. Sketch of the physical region $\Omega_s(t)$.

which can be obtained simply by replacing the integer-order diffusion term $\nabla\cdot(\widetilde{\mathbf{K}}\nabla\widetilde{u})$ by an anisotropic Riesz fractional diffusion, namely, the sum of the first two terms on the right-hand side of (2a), where the two 1D Riesz fractional derivatives are defined as follows for $1 < \alpha, \beta < 2$:

$$\frac{\partial^{\alpha}\widetilde{u}}{\partial\,|X_t|^{\alpha}} := -C_{\alpha}\left({}_{\widetilde{B}_a(Y_t)}D^{\alpha}_{X_t}\widetilde{u} + {}_{X_t}D^{\alpha}_{\widetilde{B}_b(Y_t)}\widetilde{u}\right), \tag{3a}$$

$$\frac{\partial^{\beta}\widetilde{u}}{\partial\,|Y_t|^{\beta}} := -C_{\beta}\left({}_{\widetilde{B}_c(X_t)}D^{\beta}_{Y_t}\widetilde{u} + {}_{Y_t}D^{\beta}_{\widetilde{B}_d(X_t)}\widetilde{u}\right), \tag{3b}$$

and the definitions of involved fractional Riemann-Liouville derivatives are given by

$${}_{\widetilde{B}_a(Y_t)}D^{\alpha}_{X_t}\widetilde{u} := \frac{1}{\Gamma(2-\alpha)}\frac{\partial^2\widetilde{u}}{\partial X_t^2}\int_{\widetilde{B}_a(Y_t)}^{X_t}\frac{\widetilde{u}(\xi,Y_t,t)}{(X_t-\xi)^{\alpha-1}}d\xi, \tag{4a}$$

$${}_{X_t}D^{\alpha}_{\widetilde{B}_b(Y_t)}\widetilde{u} := \frac{1}{\Gamma(2-\alpha)}\frac{\partial^2\widetilde{u}}{\partial X_t^2}\int_{X_t}^{\widetilde{B}_b(Y_t)}\frac{\widetilde{u}(\xi,Y_t,t)}{(\xi-X_t)^{\alpha-1}}d\xi. \tag{4b}$$

$${}_{\widetilde{B}_c(X_t)}D^{\beta}_{Y_t}\widetilde{u} := \frac{1}{\Gamma(2-\beta)}\frac{\partial^2\widetilde{u}}{\partial Y_t^2}\int_{\widetilde{B}_c(X_t)}^{Y_t}\frac{\widetilde{u}(X_t,\eta,t)}{(Y_t-\eta)^{\beta-1}}d\eta, \tag{4c}$$

$${}_{Y_t}D^{\beta}_{\widetilde{B}_d(X_t)}\widetilde{u} := \frac{1}{\Gamma(2-\beta)}\frac{\partial^2\widetilde{u}}{\partial Y_t^2}\int_{Y_t}^{\widetilde{B}_d(X_t)}\frac{\widetilde{u}(X_t,\eta,t)}{(\eta-Y_t)^{\beta-1}}d\eta, \tag{4d}$$

$$C_{\alpha} := \frac{1}{2\cos\left(\frac{\pi\alpha}{2}\right)}, \qquad C_{\beta} := \frac{1}{2\cos\left(\frac{\pi\beta}{2}\right)}. \tag{4e}$$

Moreover, $\widetilde{K}_X$ and $\widetilde{K}_Y$ are two positive constants and they represent the x- and y-components of Lagrangian diffusion matrix $\widetilde{\mathbf{K}} = \mathrm{diag}\{\widetilde{K}_X, \widetilde{K}_Y\}$.

The following initial conditions are prescribed for system (2):

$$\widetilde{u}(\mathbf{X},0) = \widetilde{u}_0(\mathbf{X},0) \qquad \forall\,\mathbf{X}\in\Omega_s(0), \tag{5a}$$

$$\widetilde{v}(\mathbf{X},0) = \widetilde{v}_0(\mathbf{X},0) \qquad \forall\,\mathbf{X}\in\Omega_s(0), \tag{5b}$$

which specify the values of the Lagrangian transmembrane potential and recovery variable at the initial time $t = 0$.

Finally, to close system (2), we also need to impose some boundary condition for $\widetilde{u}$. To the end, we divide the whole boundary $\Gamma_{\Omega_s}(t)$ of the structure $\Omega_s(t)$ into the Dirichlet part $\Gamma_D(t)$ and the Neumann part $\Gamma_N(t)$, hence, $\Gamma_{\Omega_s}(t) = \Gamma_D(t)\cup\Gamma_N(t)$. Let $\mathbf{n}$ denote the outward normal to $\Gamma_{\Omega_s}(t)$. We then impose the following mixed boundary condition on $\widetilde{u}$:

$$\widetilde{u}(\mathbf{X},t) = g_1(\mathbf{X},t) \qquad \forall\,\boldsymbol{\chi}(\mathbf{X},t)\in\Gamma_D(t), \quad t\in(0,T), \tag{6a}$$

$$\frac{\partial\widetilde{u}(\mathbf{X},t)}{\partial\mathbf{n}} = g_2(\mathbf{X},t) \qquad \forall\,\boldsymbol{\chi}(\mathbf{X},t)\in\Gamma_N(t), \quad t\in(0,T), \tag{6b}$$

where g_1 and g_2 are two given scaler-valued functions which are defined on $\Gamma_D(t)$ and $\Gamma_N(t)$, respectively.

To sum up, the initial-boundary value problem, which defines the fractional FitzHugh-Nagumo monodomain model and will be solved in this paper, consists of equations (2), (5) and (6).

From (4), we see that the Riemann-Liouville derivatives are domain-dependent, since the physical domain $\Omega_s(t)$ is irregular and also changes in time, this makes the limits of the integrals in (4) also change in time. As a result, numerical discretizations of the Riesz fractional derivatives in 2D on such an irregular moving domain is not only complicated and expensive but also challenging. In the next section, we shall propose a ghost structure reformulation of the above monodomain model so that the computational domain will be a fixed rectangle, consequently, the Riesz fractional derivatives become cleanly defined with fixed limits in the integrals, which in turn can be efficiently discretized.

3. Formulation of the ghost structure method

The original ghost structure (GS) method was proposed in [8] for solving the monodomain equation and simulate the action potential(AP) propagation in a heart. In the GS formulation, the membrane dynamics, including the ion concentration and stimulation current density, are described using the Lagrangian coordinates, while the transmembrane potential is described using the Eulerian coordinates. The interchange between the Lagrangian variables and the Eulerian variables is achieved by an integral transformation which involves a delta function. As a result, the GS method can handle effectively the AP propagation problem in a complexly deformed heterogeneous structure such as a heart by the finite different method.

The goal of this section is to extend the GS method for the integer-order FHN monodomain model to the fractional FHN monodomain model. Specifically, we shall derive a GS formulation for the fractional FHN monodomain model (2), (5), (6). As expected, the complexity and non-locality of fractional operators will cause some difficulties in deriving its GS reformulation. On the other hand, since the GS formulation employs a fixed rectangular computational domain, it significantly simplifies the definition and computation of the fractional derivatives appear in the model because there is no need to deal with variable limits in the Riemann-Liouvlle fractional derivatives given in (2a). Hence, the GS formulation has a clear advantage to handle fractional differential equations in two or higher dimensions.

3.1. Computational domain and ghost region extension

The first step in the GS formulation is to choose a computational domain, usually a rectangular domain, which strictly contains the structure over the whole computational time interval $0 < t \le T$. The complement of the structure region in the computational domain is called the ghost region, and the interface between the structure region and the ghost region is the boundary of the structure. Then the next step is to give an appropriate extension of the materials properties of the structure and functions defined on it into the boundary and ghost region, which will be done using a delta function technique.

Figure 2(a) shows the whole computational domain denoted by $D = [B_a, B_b] \times [B_c, B_d]$, where $x = B_a$ and $x = B_b$ describe, respectively, the left and right edges of D, and $y = B_c$ and $y = B_d$ represent, respectively, the bottom and top edges of D. Next, we introduce a marking function $\widetilde{\phi}(\mathbf{X}, t) : \Omega_s(0) \to [0, 1]$ such that $\widetilde{\phi}(\mathbf{X}) = 1$ whenever $\chi(\mathbf{X}, t) \in \Omega_s(t)$. By the definition of the delta function δ, we get

$$\phi(\mathbf{x}, t) = \int_{\Omega_s(t)} \widetilde{\phi}(\mathbf{X}, t)\delta\left(\mathbf{x} - \chi\left(\mathbf{X}, t\right)\right) d\mathbf{X} \qquad \forall \mathbf{x} \in D. \tag{7}$$

where $\{\mathbf{x} \in D; \phi(\mathbf{x}, t) = 1\}$ represents the structure region $\Omega_s(t)$, $\{\mathbf{x} \in D; 0 < \phi(\mathbf{x}, t) < 1\}$ indicates the boundary $\Gamma_{\Omega_s}(t)$, and $\{\mathbf{x} \in D; \phi(\mathbf{x}, t) = 0\}$ represents the ghost region. Set $\Omega_{ex}(t) := D - \Omega_s(t) \cup \Gamma_{\Omega_s}(t)$.

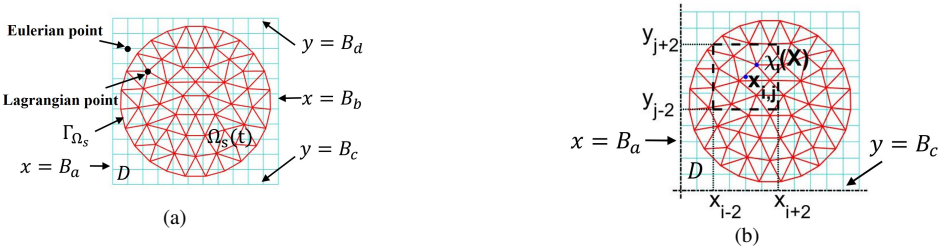

Fig. 2. (a) shows the sketch of the computational domain for the GS method; (b) shows the sketch of the fast algorithm.

In this paper, we assume that each part of the regions consists of a uniformly distributed propagation medium and use $\mathbf{K}_s$ and $\mathbf{K}_{boun}$ to denote the Eulerian diffusion coefficients in $\Omega_s(t)$ and on $\Gamma_{\Omega_s}(t)$, respectively. Then, the global Eulerian diffusion coefficient $\mathbf{K}(\mathbf{x})$ in D can be expressed as

$$\mathbf{K}(\mathbf{x}) = \phi(\mathbf{x}, t)\,\mathbf{K}_s + (1 - \phi(\mathbf{x}, t))\,\mathbf{K}_{boun} \qquad \forall \mathbf{x} \in D. \tag{8}$$

Since the Eulerian transmembrane potential u and Eulerian recovery variable v are defined in the whole computational domain D in the Eulerian coordinates and their counterparts $\widetilde{u}$ and $\widetilde{v}$ in the Lagrangian coordinates are only defined in the structure region $\Omega_s(t)$, we need to have some efficient conversion formulas for computing u and v from $\widetilde{u}$ and $\widetilde{v}$. Below we present a strategy for achieving this goal using the boundary values of $\widetilde{u}$ and $\widetilde{v}$ on $\Gamma_{\Omega_s}(t)$. We shall use u as an example to describe the detailed extension procedure.

For any $\mathbf{x} \in \Omega_{ex}(t) \cup \Gamma_{\Omega_s}(t)$, we first determine the Lagrangian point $\mathbf{X}$ on the boundary Γ_{Ω_s} which is closest to $\mathbf{x}$ and set

$$\mathbb{X}_{\min} = \left\{\mathbf{X} \in \Gamma_{\Omega_s(t)};\ \|\boldsymbol{\chi}(\mathbf{X}, t) - \mathbf{x}\|_2 \text{ is minimized}\right\}.$$

If there are m boundary points in $\mathbb{X}_{\min}$, say, $\mathbb{X}_{\min} = \{\mathbf{X}_1, \mathbf{X}_2, \cdots, \mathbf{X}_m\}$, we define the approximate transmembrane potential at x to be the average value of $\widetilde{u}$ over $\mathbb{X}_{\min}$, denoted by

$$u_{ave}(\mathbf{x}) = \frac{1}{m}\sum_{p=1}^{m} \widetilde{u}|_{\Gamma_{\Omega_s}(t)}(\mathbf{X}_p).$$

The extension of the Eulerian variable in the ghost region can be obtained by using $u_{ave}(\mathbf{x})$. To ensure the continuity of the variable in the computational domain D after being extended to the ghost domain, the variable in the boundary domain $\Gamma_{\Omega_s}(t)$ should be modified by using $\phi(\mathbf{x}, t)$ and $u_{ave}(\mathbf{x})$.

Then we have

$$u(\mathbf{x}, t) := \begin{cases} u(\mathbf{x}, t) & \text{if } \mathbf{x} \in \Omega_s(t),\ t \in (0, T), \\ \phi(\mathbf{x}, t)\,u(\mathbf{x}, t) + (1 - \phi(\mathbf{x}, t))\,u_{ave}(\mathbf{x}) & \text{if } \mathbf{x} \in \Gamma_{\Omega_s}(t),\ t \in (0, T), \\ u_{ave}(\mathbf{x}) & \text{if } \mathbf{x} \in \Omega_{ex}(t),\ t \in (0, T). \end{cases} \tag{9}$$

On the boundary $\Gamma_{GD}(t)$ of the regular ghost computational domain D, we impose the following (artificial) homogeneous Dirichlet boundary condition:

$$u(\mathbf{x}, t) = 0 \qquad \forall \mathbf{x} \in \Gamma_{GD}(t),\ t \in (0, T). \tag{10}$$

We also need to extend the definitions of the Riesz and Riemann-Louville fractional derivatives to the computational domain D, which can be done easily by changing the limits of the integrations in the previous definitions (4). Then, the new Riesz and Riemann-Louville fractional derivatives $\frac{\partial^\alpha u}{\partial |x|^\alpha}$ and $\frac{\partial^\beta u}{\partial |y|^\beta}$ are defined as follows:

$$\frac{\partial^\alpha u}{\partial |x|^\alpha} = -C_\alpha \left({}_{B_a}D_x^\alpha u + {}_x D_{B_b}^\alpha u\right), \tag{11a}$$

$$\frac{\partial^\beta u}{\partial |y|^\beta} = -C_\beta \left({}_{B_c}D_y^\beta u + {}_y D_{B_d}^\beta u\right), \tag{11b}$$

where for $1 < \alpha, \beta < 2$

$${}_{B_a}D_x^\alpha u := \frac{1}{\Gamma(2-\alpha)}\frac{\partial^2 u}{\partial x^2}\int_{B_a}^{x} \frac{u(\xi, y, t)}{(x-\xi)^{\alpha-1}} d\xi, \tag{12a}$$

$${}_x D_{B_b}^\alpha u := \frac{1}{\Gamma(2-\alpha)}\frac{\partial^2 u}{\partial x^2}\int_{x}^{B_b} \frac{u(\xi, y, t)}{(\xi-x)^{\alpha-1}} d\xi. \tag{12b}$$

$${}_{B_c}D_y^\beta u := \frac{1}{\Gamma(2-\beta)}\frac{\partial^2 u}{\partial y^2}\int_{B_c}^{y} \frac{u(x, \eta, t)}{(y-\eta)^{\beta-1}} d\eta, \tag{12c}$$

$${}_y D_{B_d}^\beta u := \frac{1}{\Gamma(2-\beta)}\frac{\partial^2 u}{\partial y^2}\int_{y}^{B_d} \frac{u(x, \eta, t)}{(\eta-y)^{\beta-1}} d\eta, \tag{12d}$$

$$C_\alpha := \frac{1}{2\cos\left(\frac{\pi\alpha}{2}\right)}, \qquad C_\beta := \frac{1}{2\cos\left(\frac{\pi\beta}{2}\right)}. \tag{12e}$$

Thus, the coefficients of the partial differential equation with the spacial fractional operators can be easily obtained without considering the complicated geometry of the real moving structure.

3.2. The governing equations of the ghost structure method

Summing up the above setup, we have transformed the original fractional moving boundary monodomain model into a fractional PDE problem with variable coefficients on a fixed domain. Specifically, the governing equations of the GS method for our fractional monodomain model is given as follows:

$$\frac{\partial u}{\partial t} = K_x(\mathbf{x})\frac{\partial^\alpha u}{\partial |x|^\alpha} + K_y(\mathbf{x})\frac{\partial^\beta u}{\partial |y|^\beta} + I_{\text{ion}}(u, v) \quad \text{in } D \times (0, T), \tag{13a}$$

$$\widetilde{u}(\mathbf{X}, t) = \int_D u(\mathbf{x}, t)\delta\left(\mathbf{x} - \boldsymbol{\chi}\left(\mathbf{X}, t\right)\right)d\mathbf{x} \quad \text{in } \Omega_s(t) \times (0, T), \tag{13b}$$

$$\frac{\partial \widetilde{v}(\mathbf{X}, t)}{\partial t} = g\left(\widetilde{u}\left(\mathbf{X}, t\right), \widetilde{v}\left(\mathbf{X}, t\right)\right) \quad \text{in } \Omega_s(t) \times (0, T), \tag{13c}$$

$$v(\mathbf{x}, t) = \int_{\Omega_s(t)} \widetilde{v}(\mathbf{X}, t)\delta\left(\mathbf{x} - \boldsymbol{\chi}\left(\mathbf{X}, t\right)\right)d\mathbf{X} \quad \text{in } D \times (0, T). \tag{13d}$$

In the above system, the Eulerian transmembrane potential u and Eulerian recovery variable v are described in the Eulerian coordinates; while the Lagrangian transmembrane potential $\widetilde{u}$ and Lagrangian recovery variable $\widetilde{v}$ are described in the Lagrangian coordinates. $\Omega_s(t)$ represents the moving structure which is immersed in the larger computational domain D. The above system is also subject to the initial condition (5) and the boundary condition (10) as well as the internal (interface) condition (6), which then gives a complete fractional order initial-boundary value problem. During diastolic filling and systolic contraction, heart is subjected to large deformation. The fractional FitzHugh-Nagumo monodomain model does not include an equation used to update the coordinates of the Lagrange points. In this paper, the deformation and the displacement of heart are obtained by using the nuclear magnetic resonance images. In the future, we intend to determine the deformation and the displacement of heart by simulating the fluid-structure coupling system. The procedure of solving the fractional FHN monodomain model will be introduced in Section 4.

4. Numerical method

Since the Eulerian transmembrane potential u and Eulerian recovery variable v are described in the Eulerian coordinates, it is natural to compute them on a fixed regular Cartesian grid. On the other hand, the transmembrane potential $\widetilde{u}$ and recovery variable $\widetilde{v}$ are described in the Lagrangian coordinates, they must be computed at the corresponding Lagrangian points. The transformation between the Eulerian and Lagrangian coordinates is done by an integral transformation which involves a delta function as given in (13b) and (13d). Moreover, since the initial conditions are given for the transmembrane potential $\widetilde{u}$ and recovery variable $\widetilde{v}$ at the Lagrangian points in the structure, it is necessary first to generate the initial values for the transmembrane potential u and recovery variable v at the Eulerian points in the whole computational domain D using the transformation formula (13d), which then allows us to solve the fractional FHN monodomain model in the whole computational domain D.

One of the main advantages of the GS method is its ability to effectively handle problems with complex boundaries using equations (13b) and (13d) which involve a delta function. This advantage becomes even more significant for solving fractional FHN monodomain model because it allows us to avoid evaluating complicated domain-dependent fractional partial derivatives.

Below we propose the following algorithm/procedure to solve the fractional FHN monodomain model: first, we use a combined implicit-explicit Euler scheme and third order total variation diminishing (TVD) Runge-Kutta scheme for the time discretization; second, at each time step, we use the finite difference method for the spatial discretization to compute the Eulerian transmembrane potential $u(\mathbf{x}, t)$ by solving equation (13a) and to convert $u(\mathbf{x}, t)$ into the Lagrangian transmembrane potential by equation (13b); finally, we calculate the Lagrangian recovery variable by equation (13c), and then convert $\widetilde{v}(\mathbf{X}, t)$ into the Eulerian recovery variable by equation (13d) for updating the Eulerian transmembrane potential at the next time step. For the moving structure, before updating the Eulerian transmembrane potential at the next step, we also need to use $\widetilde{u}(\mathbf{X}, t)$ to reassign the $u(x, t)$ in the same way as $\widetilde{v}(\mathbf{X}, t)$ does.

4.1. Time discretization

Various time-stepping schemes, such as explicit scheme, implicit schemes, implicit-explicit schemes etc. can be used for the time discretization. Explicit schemes are easy to implement but require stringent mesh conditions in order to ensure the stability of the numerical schemes. On the other hand, implicit schemes allow the use of large mesh sizes but require to solve nonlinear algebraic systems at each time step, which is expensive especially for the large-scale nonlinear problems. In this paper, we take the middle road by using the implicit-explicit schemes, in which the linear terms are treated implicitly and the nonlinear terms explicitly in time. Thus, only linear systems are solved at each time step under some mild mesh conditions. Let $\{t_n\}_{n=1}^N$ be a uniform partition of $[0, T]$ with time step size $\Delta t \in (0, 1)$, where N is a positive integer, hence, $\Delta t := T/N$. We propose the following implicit-explicit Euler time-stepping scheme for the nonlinear equation (13a): for $n = 1, 2, \cdots, N$,

$$u^n - \Delta t \left[K_x(\mathbf{x}) \frac{\partial^\alpha u^n}{\partial |x|^\alpha} + K_y(\mathbf{x}) \frac{\partial^\beta u^n}{\partial |y|^\beta} \right] = \Delta t \, I_{\text{ion}}(u^{n-1}, v^{n-1}) + u^{n-1} \quad \text{in } D. \tag{14}$$

It is easy to verify that the truncation error of the above implicit-explicit Euler scheme is of order $O(\Delta t)$, which is consistent with the numerical results in **Test 1**.

In (13c), the function g is nonlinear in $\widetilde{u}$ and $\widetilde{v}$ that relates the ionic flux to the total ionic current. In order to maintain the stability and accuracy, we discretize (13c) using the third-order TVD Runge-Kutta method (cf. [36]) although other schemes can also be employed. For $n = 1, 2, \cdots, N$, we define

$$\widetilde{v}^{n-1,1} = \widetilde{v}^{n-1} + \Delta t g(\widetilde{u}^n, \widetilde{v}^{n-1}), \tag{15a}$$

$$\widetilde{v}^{n-1,2} = \widetilde{v}^{n-1,1} + \frac{\Delta t}{4} \left[-3g(\widetilde{u}^n, \widetilde{v}^{n-1}) + g(\widetilde{u}^n, \widetilde{v}^{n-1,1}) \right], \tag{15b}$$

$$\widetilde{v}^{n} = \widetilde{v}^{n-1,2} + \frac{\Delta t}{12} \left[-g(\widetilde{u}^n, \widetilde{v}^{n-1}) - g(\widetilde{u}^n, \widetilde{v}^{n-1,1}) + 8g(\widetilde{u}^n, \widetilde{v}^{n-1,2}) \right]. \tag{15c}$$

The TVD Runge-Kutta method can maintain stability in the total variation seminorm, or any other seminorm or norm, of the first order Euler forward method with the same spatial discretization[37]. The TVD Runge-Kutta method mentioned above can achieve the third order accuracy, which is illustrated in [36, 37, 38].

4.2. Spatial discretization

To obtain fully discrete schemes, we also need to discretize (14) in space. To the end, let N_1 and N_2 be two positive integers, and $\Delta x := \frac{B_b - B_a}{N_1}$ and $\Delta y := \frac{B_d - B_c}{N_2}$ be the mesh sizes in x- and y-direction, respectively. Define $\mathbf{x}_{i,j} := (B_a + i\Delta x, B_c + j\Delta y)$ for $i = 0, 1, \cdots, N_1$ and $j = 0, 1, \cdots, N_2$, which gives a Cartesian grid over D. As expected, a key component of a space discretization for (14) is to design efficient approximation formulas for computing the Riesz fractional derivatives appear in the equation. Here we adopt the fractional central difference scheme proposed in [35, 39] to do the job. The spatial truncation error of the fractional central difference scheme is proved in [39], which is consistent with the results in the **Test 1**. Then, the Riesz fractional derivative can be discretized as the following approximation formulas:

$$\frac{\partial^\alpha u\left(x_i, y_j, t_k\right)}{\partial |x|^\alpha} = -\frac{1}{\Delta x^\alpha} \sum_{p=-N_1+i}^{i} g_p^\alpha u\left(x_{i-p}, y_j, t_k\right) + O\left(\Delta x^2\right), \tag{16}$$

$$\frac{\partial^\beta u\left(x_i, y_j, t_k\right)}{\partial |y|^\beta} = -\frac{1}{\Delta y^\beta} \sum_{p=-N_2+j}^{j} g_p^\beta u\left(x_i, y_{j-p}, t_k\right) + O\left(\Delta y^2\right), \tag{17}$$

where the coefficients g_p^α are defined by

$$g_p^\alpha = \frac{(-1)^p \, \Gamma(\alpha + 1)}{\Gamma\left(\frac{\alpha}{2} - p + 1\right) \Gamma\left(\frac{\alpha}{2} + p + 1\right)}, \qquad p = 0, \pm 1, \pm 2 \cdots$$

for which we have following facts.

Lemma 1 ([34]). *The coefficients* $\{g_p^\alpha\}_{p=-\infty}^{p=\infty}$ *defined above satisfy*

(1) $g_k^\alpha = g_{-k}^\alpha \le 0$ *and* $g_0^\alpha \ge 0$; *for all* $|k| > 0$;

(2) $\sum_{p=-\infty}^{\infty} g_p^\alpha = 0$;

(3) *for any two positive integers n and m, there holds* $\sum_{p=-m+n}^{n} g_p^\alpha > 0$.

Applying the formulas (16)–(17) to (14) we obtain the following space-time discretization of equation (13a): for $n = 1, 2, \cdots, N$,

$$u_{i,j}^n + \frac{\Delta t K_x}{\Delta x^\alpha} \sum_{p=-N_1+i}^{i} g_p^\alpha u_{i-p,j}^n + \frac{\Delta t K_y}{\Delta y^\beta} \sum_{p=-N_2+j}^{j} g_p^\beta u_{i,j-p}^n \tag{18}$$
$$= u_{i,j}^{n-1} + \Delta t\, I_{ion}\left(u_{i,j}^{n-1}, v_{i,j}^{n-1}\right), \qquad i = 0, 1, \cdots, N_1,\ j = 0, 1, \cdots N_2,$$

which gives an $N_1N_2 \times N_1N_2$ linear system for each n, and will be solved using the biconjugate gradient method [40] in our numerical tests.

4.3. Computing Lagrangian-Eulerian interaction

4.3.1. Approximating the delta function

The discretization of equations (13b) and (13d) requires to approximate the delta function. To that end, we define the following approximate 2D delta function:

$$\delta_h(\mathbf{x}) = \Psi_h(r_x)\Psi_h(r_y); \qquad r_x := \frac{x}{\Delta x}, \quad r_y := \frac{y}{\Delta y}, \tag{19}$$

where

$$\Psi_h(r) = \begin{cases} \frac{1}{2}(|r|^2 - 1)(|r| - 2), & |r| \le 1, \\ -\frac{1}{6}(|r| - 1)(|r| - 2)(|r| - 3), & 1 \le |r| \le 2, \\ 0, & \text{otherwise.} \end{cases} \tag{20}$$

We note that the above $\delta_h(\mathbf{x})$ is a regularization of a delta function proposed in [41]. For all real number r, the continuous function $\Psi_h(r)$ defined above satisfies (cf. [41])

$$\sum_{p=1,2,\ldots} \Psi_h(r - p) = 1, \tag{21a}$$

$$\sum_{p=1,2,\ldots} (r - p)\,\Psi_h(r - p) = 0, \tag{21b}$$

$$\sum_{p=1,2,\ldots} (r - p)^2\,\Psi_h(r - p) = 0. \tag{21c}$$

These formulas guarantee that constant, linear and quadratic functions can be interpolated exactly by δ_h (cf. [41]). Moreover, they ensure that the discrete delta function δ_h has the second order accuracy (cf. [41, 42, 43]).

We shall use the integral transformation of the approximate delta function to define an approximate transformation formula between Eulerian variables and Lagrangian variables. In general, the Lagrangian points must be finer than the Eulerian points to avoid leaks [43]. In order to obtain accurate approximate values for the physical quantity and to avoid overcrowding the Lagrange points, we employ an accurate Gaussian quadrature rule. To the end, we introduce a quasi-uniform triangulation $\mathcal{T}_h^n = \{\tau_e^n\}$ of $\Omega_s(0)$ and let $\left\{\mathbf{X}_l^n\right\}_{l=1}^M$ denote the nodes of $\mathcal{T}_h^n$, which are regarded as Lagrangian points. For the moving structure, the Eulerian coordinates of Lagrangian points $\left\{\mathbf{X}_l^n\right\}_{l=1}^M$ change in time.

Let $\{\phi_l^n(\mathbf{X})\}_{l=1}^M$ be the continuous piecewise linear finite element basis functions associated with $\mathcal{T}_h^n$. Then on each τ_e^n we choose the Gaussian quadrature points $\{\mathbf{X}_q^{n,e}\}_{q=1}^{N^{n,e}}$ with $\mathbf{X}_q^{n,e} \in \tau_e^n$ and denote the associated weights by $\{\omega_q^{n,e}\}_{q=1}^{N^{n,e}}$. The value of a physical quantity/function at each Gaussian point can be obtained by the finite element interpolation using the basis functions $\left\{\phi_l^n(\mathbf{X})\right\}_{l=1}^M$ and the nodal values of the function. We now use v as an example to demonstrate the procedure, that is, the approximate value of v at an Eulerian point $\mathbf{x} \in D$ is computed approximately by

$$v(\mathbf{x}, t_n) \approx \sum_{\tau_e^n \in \mathcal{T}_h^n} \sum_{q=1}^{N^{n,e}} \widetilde{v}(\mathbf{X}_q^{n,e}) \delta_h(\mathbf{x} - \boldsymbol{\chi}(\mathbf{X}_q^{n,e}, t_n)) \omega_q^{n,e}, \tag{22}$$

where $\widetilde{v}(\mathbf{X}_q^{n,e})$ is computed by the finite element interpolation as described above. Obviously, formula (22) provides a discretization for equation (13d).

Similarly, using the discrete delta function and the composite trapezoidal quadrature rule on D, we can obtain an approximate value of $\widetilde{u}$ at each Gaussian quadrature point $\mathbf{X}_q^{n,e}$ and at t_n as follows:

$$\widetilde{u}(\mathbf{X}_q^{n,e}, t_n) \approx \sum_{i,j} u(\mathbf{x}_{i,j}) \delta_h(\mathbf{x}_{i,j} - \boldsymbol{\chi}(\mathbf{X}_q^{n,e}, t_n)) \Delta x \Delta y, \tag{23}$$

where $\{\mathbf{x}_{i,j}\}$ are the Cartesian grid points introduced in Section 4.2. Formula (23) gives a discretization for equation (13b).

Finally, in order to update the recovery variable at the next time step, we need to obtain the transmembrane potential $\widetilde{u}$ at the Lagrangian point, which can be obtained by using its approximate values at the Gaussian points defined in (23) and an L^2-projection method based on the quasi-uniform triangulation $\mathcal{T}_h^n$ (cf. [31]).

In summary, our fully discrete numerical method for system (13a)-(13d) consists of (15), (18), (22), and (23).

4.3.2. Fast algorithms for computing the integral transformations of the delta function

In the GS formulation, the transformations between the Lagrangian variables and the Eulerian variables are achieved by the integral transformation formulas (13b) and (13d) which involve a delta function. Since the transformations require to evaluate the distance between the Lagrangian points and the Eulerian points, it is necessary to run time-consuming loops to compute the transformation. Notice that the value of the approximate delta function is 0 when the distance between the Lagrangian point and the Eulerian point is greater than $\min\{2\Delta x, 2\Delta y\}$. Recall that $\boldsymbol{\chi}(X, t) = (X_t, Y_t)$, define

$$i = \text{floor}\left(\frac{X_t - B_a}{\Delta x}\right), \qquad j = \text{floor}\left(\frac{Y_t - B_c}{\Delta y}\right),$$

where floor(a) stands for the integer part of a. The affected region of a Lagrangian point $\mathbf{X}$ is defined as the set/region of the Eulerian points which can be affected by the point $\mathbf{X}$. As shown in Fig. 2(b), the affected region can be determined by extending two spatial steps in both positive and negative directions along the coordinate axes from the Eulerian point $\mathbf{x}_{i,j}$. If the Eulerian points $\mathbf{x}$ is outside the region, then $\delta(x - \boldsymbol{\chi}(\mathbf{X})) = 0$. Hence, the Lagrangian point $\mathbf{X}$ is only influenced by the Eulerian points in the affected region. In order to improve the computational efficiency, we adapt two fast algorithms for the integral transformations of the delta function. The key idea of the fast algorithms is to determine the affected region and only to compute the transformations in the affected region. Algorithm 1 and 2 present the algorithmic process for solving (13b) and (13d) based on (22), and (23), respectively.

In Algorithm 1, we first determine the affected region and then use the discrete scheme (23) to obtain the Lagrangian transmembrane potential in the affected region. On the other hand, each Eulerian point $\mathbf{x}_{i,j}$ could be influenced by multiple Lagrangian points in case $\mathbf{x}_{i,j}$ is located in the affected regions of multiple Lagrangian points. In Algorithm 2, we also first determine the affected region of each Lagrangian point. Then, we obtain the converted value of the Lagrangian recovered variable at each Eulerian point $\mathbf{x}_{i,j}$ of the affected region. Thus, the Eularian recovered variable at $\mathbf{x}_{i,j}$ can be obtained by sampling over all Lagrangian points and accumulating the converted values at each Eulerian point $\mathbf{x}_{i,j}$. Since both Algorithm 1 and 2 only loop through Lagrangian points, their computational efficiency is very high.

Algorithm 1 (converting the Euler variable into the Lagrangian variable)

Require: Eulerian and Lagrangian coordinates, the Eulerian transmembrane potential
Ensure: the Lagrangian transmembrane potential

for each element $\tau_e^n \in \Omega_s(t)$ **do**
  determine the affected region
  $i = floor(\frac{X_t - B_a}{\Delta x})$
  $j = floor(\frac{Y_t - B_c}{\Delta y})$
  $i_{min} = i - 2, i_{max} = i + 2$
  $j_{min} = j - 2, j_{max} = j + 2$
  $\widetilde{u}(\mathbf{X}_q^{n,e}, t) = \sum_{i \in [i_{min}, i_{max}], j \in [j_{min}, j_{max}]} u(\mathbf{x}_{i,j}) \delta(\mathbf{x}_{i,j} - \boldsymbol{\chi}(\mathbf{X}_q^{n,e}, t)) \Delta x \Delta y$
end for

Algorithm 2 (converting the Lagrangian variable into the Euler variable)

Require: Eulerian and Lagrangian coordinates, the Lagrangian recovery variable
Ensure: the Eulerian recovery variable

$v(\mathbf{x}, t) = 0, \mathbf{x} \in D$
for each element $\tau_e^n \in \Omega_s(t)$ **do**
  determine the affected region
  $i = floor(\frac{X_t - B_a}{\Delta x})$
  $j = floor(\frac{Y_t - B_c}{\Delta y})$
  $i_{min} = i - 2, i_{max} = i + 2$
  $j_{min} = j - 2, j_{max} = j + 2$
  for $i = i_{min}$ to i_{max} **do**
    for $i = i_{min}$ to i_{max} **do**
      $v(\mathbf{x}_{i,j}, t) = v(\mathbf{x}_{i,j}, t) + \widetilde{v}(\mathbf{X}_q^{n,e}) \delta(\mathbf{x} - \boldsymbol{\chi}(\mathbf{X}_q^{n,e}, t)) \omega_q^{n,e}$
    end for
  end for
end for

5. Numerical experiments

In this section, we present five numerical tests to demonstrate the accuracy and efficiency of the proposed numerical method (and algorithms) based on the GS approach. In the first test, we analyze the errors, numerical spatial and temporal convergence orders of the proposed method by solving the Riesz fractional reaction-diffusion equation. In the second and third tests, we use the proposed method to solve the fractional FHN model first in a circular region and then in a rectangular region with four holes. In the fourth and fifth tests, we use the proposed method to solve the fractional FHN monodmoain model in the two-dimensional stationary transverse and moving longitudinal sections of a bi-ventricle heart. In neurons, the membrane potential can be influenced by the voltage-gated ion channels, while these ion channels are controlled by the membrane potential, which causes feedback loops. The feedback loops allow for complex temporal dynamics, including oscillations and regenerative events such as AP (cf. [8]). In the transverse section, we analyze the transmembrane potential propagation in a healthy heart and also in a heart with arrhythmia. In the longitudinal section, we simulate the transmembrane potential propagation during the pumping process, which requires to simulate the model in the moving longitudinal section of a ventricle. Since the initial condition of the transmembrane potential is given at the Lagrangian points in the structure region, it is necessary to first obtain the transmembrane potential at the Eulerian point in the computational domain D by using an integral transformation which involves a delta function, and then to solve the fractional FHN monodomain model. All our simulations are performed on a Windows workstation with Intel(R) Xeon(R) Gold 5122 (4 cores, 3.60GHz, 64GB memory), and implemented in PETSc [44].

Test 1. We firstly consider the following two-dimensional Riesz fractional reaction-diffusion equation:

$$\frac{\partial u}{\partial t} = K_x \frac{\partial^\alpha u}{\partial |x|^\alpha} + K_y \frac{\partial^\beta u}{\partial |y|^\beta} + F(u) + v \quad \text{in } D \times (0,T), \tag{24}$$

with the initial condition

$$\widetilde{u}(\mathbf{X},0) = 10X^2(1-X)^2 Y^2 (1-Y)^2 \quad \text{in } \Omega_s(0),$$

and the boundary condition

$$\widetilde{u}(\mathbf{X},t) = 0 \qquad \text{if } \boldsymbol{\chi}(\mathbf{X},t) \in \Gamma_{\Omega_s}(t),$$

where $F(u) = -u^2$, and

$$\begin{aligned}
\widetilde{v}(\mathbf{X},t) &= -10e^{-t}X^2(1-X)^2 Y^2(1-Y)^2 + 100e^{-2t}X^4(1-X)^4 Y^4(1-Y)^4 \\
&\quad + 10K_x C_\alpha e^{-t} Y^2(1-Y)^2 (q(X,\alpha) + q(1-X,\alpha)) \\
&\quad + 10K_y C_\beta e^{-t} X^2(1-X)^2 (q(Y,\beta) + q(1-Y,\beta)) \quad \text{in } \Omega_s(t) \times (0,T), \\
q(X,\theta) &= \frac{\Gamma(5)}{\Gamma(5-\theta)} X^{4-\theta} - \frac{2\Gamma(4)}{\Gamma(4-\theta)} X^{3-\theta} + \frac{\Gamma(3)}{\Gamma(3-\theta)} X^{2-\theta}.
\end{aligned}$$

The rectangular region $\Omega_s(t) \equiv [0,1] \times [0,1]$, which is stationary in t. The regular ghost structure region(i.e., the computational domain) is taken as $D = [-0.1, 1.1] \times [-0.1, 1.1]$ which contains $\Omega_s(t)$. The model parameters are chosen as $K_x(\mathbf{x}) = K_y(\mathbf{x}) \equiv 1$ in $\Omega_s(t)$.

The exact solution of the Riesz fractional reaction-diffusion equation(24) is

$$\widetilde{u}(\mathbf{X},t) = 10e^{-t}X^2(1-X)^2 Y^2(1-Y)^2 \quad \text{in } \Omega_s(t). \tag{25}$$

Table 1 gives the errors and spatial convergence orders for different norms at $t = 1$. The errors and temporal convergence orders are given in Table 2. The numerical results show that spatial and temporal convergence orders are close to 2 and 1, respectively.

Test 2. We consider the fractional FHN monodomain model (13) with following source functions:

$$\begin{aligned}
I_{\text{ion}}(u,v) &= \lambda(u(1-u)(u-\theta) - v + I_{\text{sti}}), \\
g(\widetilde{u},\widetilde{v}) &= \epsilon(a\widetilde{u} - b\widetilde{v} - c);
\end{aligned}$$

Table 1. Errors and spatial convergence orders of the GS method with $\Delta t = 10^{-4}$

	$\Delta x = \Delta y$	L^2 error	Order	L^∞ error	Order
$\alpha = \beta = 1.8$	0.1	9.8699e-03	-	1.9476e-03	-
	0.05	3.8267e-03	1.3669	4.0642e-04	2.2606
	0.025	1.1344e-03	1.7542	7.1922e-05	2.4985
	0.0125	3.9354e-04	1.5273	2.6823e-05	3.4285
$\alpha = 1.8, \beta = 1.5$	0.1	9.4208e-03	-	1.7875e-03	-
	0.05	3.9626e-03	1.2494	4.1749e-04	2.0981
	0.025	1.2558e-03	1.6578	7.8742e-05	2.4069
	0.0125	3.5352e-04	1.8288	2.4500e-05	4.0575

Table 2. Errors and temporal convergence orders of the GS method with $\Delta x = \Delta y = 0.025$

	Δt	L^2 error	Order	L^∞ error	Order
$\alpha = \beta = 1.8$	0.1	4.0717e-02	-	2.0135e-03	-
	0.05	2.4176e-02	0.7520	1.0838e-03	0.8936
	0.025	1.4513e-02	0.7361	5.6951e-04	0.9283
	0.0125	8.3726e-03	0.7936	3.0107e-04	0.9196
$\alpha = 1.8, \beta = 1.5$	0.1	4.3038e-02	-	2.0917e-03	-
	0.05	2.5731e-02	0.7421	1.1487e-03	0.8647
	0.025	1.5491e-02	0.7320	6.4191e-04	0.8396
	0.0125	9.1138e-03	0.7654	3.5147e-04	0.8690

and initial conditions

$$\widetilde{u}(\mathbf{X},0) = \begin{cases} 1, & r - \sqrt{r^2-(r-Y)^2} < X \le r \text{ and} \\ & r - \sqrt{r^2-(r-X)^2} < Y \le r \qquad \forall \mathbf{X} \in \Omega_s(0), \\ 0, & \text{otherwise}, \end{cases}$$

$$\widetilde{v}(\mathbf{X},0) = \begin{cases} 0.1, & r - \sqrt{r^2-(r-Y)^2} < X < r + \sqrt{r^2-(r-Y)^2} \\ & \text{and } r \le Y < r + \sqrt{r^2-(r-X)^2} \qquad \forall \mathbf{X} \in \Omega_s(0), \\ 0, & \text{otherwise}, \end{cases}$$

where $r = 1.25$ and the boundary conditions

$$\widetilde{u}(\mathbf{X},t) = 0 \qquad \text{if } \boldsymbol{\chi}(\mathbf{X},t) \in \Gamma_{\Omega_s}(t),$$
$$\widetilde{v}(\mathbf{X},t) = 0 \qquad \text{if } \boldsymbol{\chi}(\mathbf{X},t) \in \Gamma_{\Omega_s}(t).$$

The model parameters are chosen as $\lambda = 1$, $\theta = 0.1$, $\epsilon = 0.01$, $a = 0.5$, $b = 1$, $c = 0$. $\widetilde{I}_{\text{sti}}$ is an imposed Lagrangian stimulation current. Since the external stimulus is not taken into account in this test, hence, $I_{\text{sti}} = 0$. $\Omega_s(t)$ represents the circular structure given by

$$\Omega_s(t) \equiv \{(x,y);\ (x-1.25)^2 + (y-1.25)^2 \le (1.25)^2\},$$

which does not change in time, and the regular ghost structure region (i.e., the computational domain) is chosen as $D = [-0.1, 2.6] \times [-0.1, 2.6]$, which obviously contains $\Omega_s(t)$. This model is known to produce a stable spiral wave and relevant computational results of this test problem can be found in [35].

To ensure the consistency with the spatial mesh sizes in references [23, 34], we choose $\Delta x = \Delta y = \frac{2.5}{256}$ in this test, which results in partitioning the computational domain D into 277×277 grids. The time step size $\Delta t = 0.1$ is used. Also, in this test we only consider equal order fractional derivatives, that is, $\alpha = \beta$.

Table 3. The CPU time running up to $t = 1000$

	$\alpha = \beta = 1.6$ $K_x = K_y = 10^{-4}$	$\alpha = \beta = 1.8$ $K_x = K_y = 10^{-4}$	$\alpha = \beta = 1.8$ $K_x = 10^{-4}$ $K_y = 0.25 \times K_x$	$\alpha = \beta = 1.8$ $K_y = 10^{-4}$ $K_x = 0.25 \times K_y$
GS method	685.59s	691.74s	686.86s	688.41s
Liu et al[35]	662.77s	655.14s	662.34s	663.06s

We first consider the isotropic case in which $K_x(\mathbf{x}) = K_y(\mathbf{x}) = 10^{-4}$ for all $\mathbf{x} \in \Omega_s(t)$. Fig. 3 displays the computed solutions at $t = 1000$ for different α, in each scenario, a stable spiral wave of the rotation solution is clearly observed, in fact, the wave generates a clockwise rotation curve. When $\alpha = \beta = 1.8$, Fig. 3(a) shows the spiral waves obtained by the numerical method of this paper, as a comparison, Fig. 3(b) displays the computed solution of the same model obtained by the method of [35]. When $\alpha = \beta = 1.6$, Fig. 3(c) and Fig. 3(d) show the computed spiral waves obtained by the method of this paper and in [35], respectively. We also observe from Fig. 3 that the width of the spiral wave decreases as α and β decrease. When $\alpha = \beta = 1.8$, the average width of the spiral wave is 0.16, which is wider than the average width 0.09 when $\alpha = \beta = 1.6$.

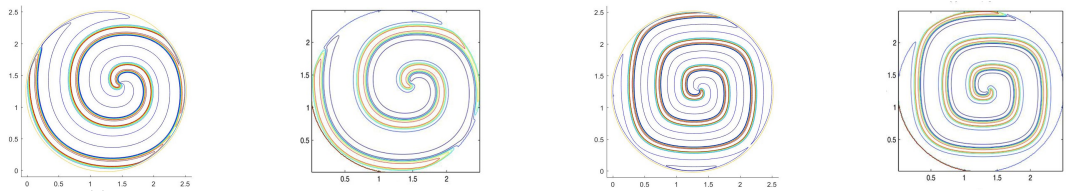

Fig. 3. Test 2. Spiral wave solutions of the fractional FNH model at $t = 1000$ with $K_x = K_y = 10^{-4}$ and $\alpha = \beta$: (a) computed solution by the method of this paper with $\alpha = 1.8$; (b) computed solution by the method of [35] with $\alpha = 1.8$; (c) computed solution by the method of this paper with $\alpha = 1.6$; (d) computed solution by the method of [35] with $\alpha = 1.6$.

Next, we consider the anisotropic diffusion case in which $K_x(\mathbf{x}) \not\equiv K_y(\mathbf{x})$. Fig. 4 gives the numerical results obtained by the method of this paper and that by [35], respectively, with $\alpha = \beta = 1.8$ and $t = 1000$. When $K_x(\mathbf{x}) = 10^{-4}$, $K_y(\mathbf{x}) = 0.25 \times K_x(\mathbf{x})$ for all $\mathbf{x} \in \Omega_s(t)$, Fig. 4(a) and Fig. 4(b) show the results obtained by the method of this paper and that by [35], respectively. When $K_y(\mathbf{x}) = 10^{-4}$, $K_x(\mathbf{x}) = 0.25 \times K_y(\mathbf{x})$ for all $\mathbf{x} \in \Omega_s(t)$, the computed results obtained by method of this paper and that by [35] are given in Fig. 4(c) and Fig. 4(d), respectively. We observe from Fig. 4 that in the anisotropy case, the spiral wave generated by the fractional FHN model in the circular region appears elliptical, and the diffusion coefficient component in the long axis direction of the ellipse is larger than that in the short axis direction. Table 3 shows the CPU time of different methods. The CPU time required by our method is comparable to that required by the method in [35].

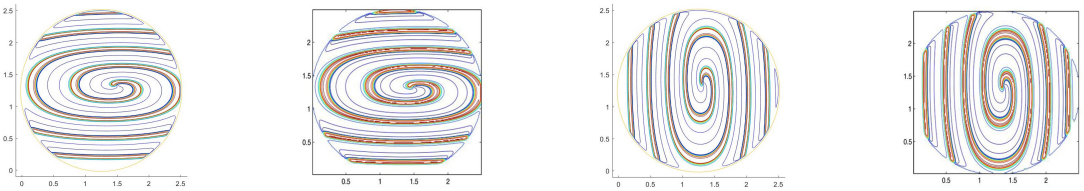

Fig. 4. Test 2. Spiral wave solutions of the fractional FHN model at $t = 1000$ with $\alpha = \beta = 1.8$: (a) $K_x = 10^{-4}$, $K_y = 0.25 \times K_x$, computed solution by the method of this paper; (b) computed solution by the method of [35]; (c) $K_y = 10^{-4}$, $K_x = 0.25 \times K_y$, computed solution by the method of this paper; (d) computed solution by the method of [35].

Test 3. We consider the same fractional FHN monodomain model as in **Test 2** but with different initial and

boundary conditions which are given below.

$$\widetilde{u}(X, Y, 0) = \frac{1}{1 + \exp(50((X^2 + Y^2)^{\frac{1}{2}} - 0.1))} \qquad \text{in } \Omega_s(0),$$
$$\widetilde{v}(X, Y, 0) = 0 \qquad \text{in } \Omega_s(0);$$

and the homogeneous Neumann boundary condition

$$\frac{\partial \widetilde{u}(\mathbf{X})}{\partial \mathbf{n}} = 0 \qquad \text{if } \boldsymbol{\chi}(\mathbf{X}, t) \in \Gamma_{\Omega_s}(t),$$
$$\frac{\partial \widetilde{v}(\mathbf{X})}{\partial \mathbf{n}} = 0 \qquad \text{if } \boldsymbol{\chi}(\mathbf{X}, t) \in \Gamma_{\Omega_s}(t),$$

where $\Omega_s(t) \equiv [0, 1] \times [0, 1]$ minus four holes of radius 0.1, see Fig. 5. Again, $\Omega_s(t)$ is stationary in t. The regular ghost structure region (i.e., the computational domain) is taken as $D = [-0.04, 1.04] \times [-0.04, 1.04]$ which contains $\Omega_s(t)$. In this test, the model parameters are chosen as $\lambda = 100$, $\theta = 0.25$, $\epsilon = 1$, $a = 0.16875$, $b = 1$, $c = 0$, and $K_x(\mathbf{x}) = K_y(\mathbf{x}) \equiv 0.01$ in $\Omega_s(t)$. It is known that the transmembrane potential will propagate from the lower left corner of the structure to the whole structure, and it bypasses the four holes along the way during the propagation. Relevant numerical results of this test problem can be found in reference [45].

In this test, the spatial mesh sizes are chosen as $\Delta x = \Delta y = \frac{1}{256}$ and the time step size as $\Delta t = 0.2\Delta x$, which results in partitioning the computational domain D into 277×277 grids. Also, in this test we only consider equal order fractional derivatives, that is, $\alpha = \beta$.

Figs. 5(a)-5(d) and Figs. 5(e)-5(h) show numerical results with $\alpha = \beta = 2$ obtained by the method of this paper and that by [45], respectively. In order to analyze the arrhythmia, the following external stimulus is applied in the central region of the structure at time $t = 4$:

$$\widetilde{I}_{\text{sti}}(\mathbf{X}, 4) = \begin{cases} 1, & (X_4 - 0.5)^2 + (Y_4 - 0.5)^2 < (0.2)^2 \text{ and } (X_4, Y_4) \in \Omega_s(4), \\ 0, & \text{otherwise.} \end{cases} \tag{26}$$

Under the influence of the above external stimulation, the transmembrane potential begins to propagate cyclically in the structure $\Omega_s(t)$. From Fig. 5, we see that the numerical results obtained by the method of this paper are in agreement with those obtained in [45].

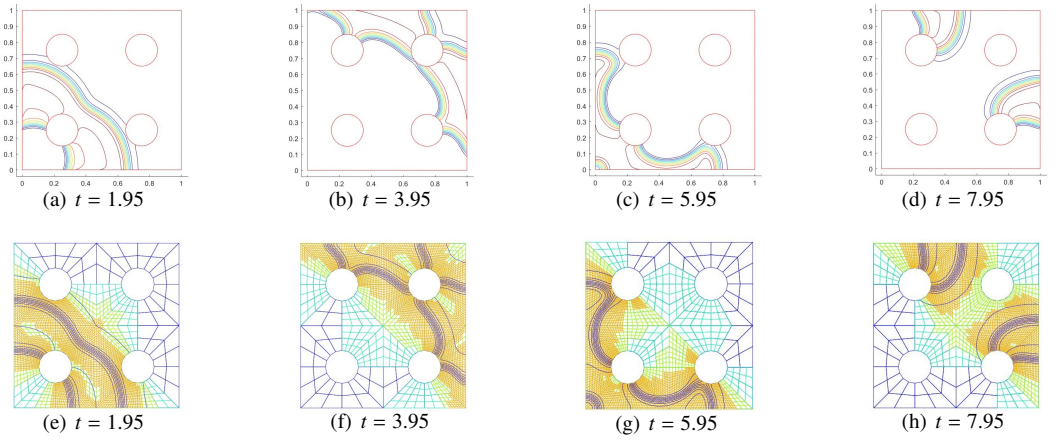

(a) $t = 1.95$ (b) $t = 3.95$ (c) $t = 5.95$ (d) $t = 7.95$

(e) $t = 1.95$ (f) $t = 3.95$ (g) $t = 5.95$ (h) $t = 7.95$

Fig. 5. Test 3: The numerical solutions of the fractional FHN model with $\alpha = \beta = 2$ at different time points: (a)-(d) are obtained by the method of this paper; (e)-(h) are obtained by the method of [45].

For $\alpha = \beta = 1.8$, Figs. 6(a)-6(d) display the numerical results obtained by the proposed method. Compared to Figs. 5 and 6, we see that the propagation velocity of the transmembrane potential gradually decreases as α decreases. Due to the slow-down of the propagation, the transmembrane potential covers the external stimulation. As shown in Fig. 6, the transmembrane potential spreads from the lower left corner, bypasses the four holes, and finally disappears

in the upper right corner. Thus, the external stimulation does not affect the transmission path of the transmembrane potential when the potential covers the external stimulation. For $\alpha = 1.8$ and $\alpha = 2.0$, the CPU time running up to $t = 5$ are $889.23s$ and $930.76s$, respectively.

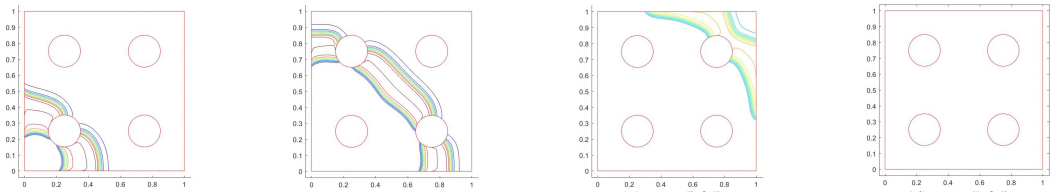

(a) $t = 1.95$ (b) $t = 3.95$ (c) $t = 5.95$ (d) $t = 7.95$

Fig. 6. Test 3: The numerical solutions of the fractional FHN monodomain model with $\alpha = \beta = 1.8$ at different time points obtained by the method of this paper.

Test 4. The same fractional FHN monodomain model (i.e., the same model parameters are assumed, isotropic) as in **Test 3** is considered in this test to simulate the transmembrane potential propagation in a two-dimensional transverse section of the ventricle $\Omega_s(t)$, the so-called short-axis view, with both left and right ventricles as shown in Fig. 7. The transverse section $\Omega_s(t)$ is placed into the ghost structure region which is taken as $D = [-0.25, 10.25] \times [-0.25, 8.75]$. The biological ramification is to simulate the transmembrane potential propagation in a healthy heart or in a heart with arrhythmia. The homogeneous Neumann boundary condition on $\Gamma_{\Omega_s}(t)$ is imposed, and the initial conditions are chosen as

$$\widetilde{u}(\mathbf{X}, 0) = \frac{1}{1 + \exp(50((X - 5.5)^2 + (Y - 1.75)^2)^{\frac{1}{2}} - 0.5))} \quad \text{in } \Omega_s(0),$$
$$\widetilde{v}(\mathbf{X}, 0) = 0 \quad \text{in } \Omega_s(0).$$

It is known that the transmembrane potential begins to diffuse from the source and travels within the myocardium to the entire heart wall [46].

In this test, the spatial mesh sizes are chosen as $\Delta x = \Delta y = 0.025$ and the time step size as $\Delta t = 0.2\Delta x$, which results in partitioning the computational domain D into 420×360 grids.

Fig. 7 shows the numerical results for $\alpha = \beta = 2$ and $\alpha = \beta = 1.8$. Comparing Figs. 7(a)-7(d) with Figs. 7(e)-7(h), we observe that the propagation velocity of the transmembrane potential on the transverse section of the heart gradually decreases as α decreases. When $\alpha = 2$, the propagation time of the transmembrane potential is about 37.75 (unit-less), while the required time is 66.25 (unit-less) when $\alpha = 1.8$. Moreover, the wave width also decreases with the decrease of α. When $\alpha = 2$, the average wave width during propagation is 0.24 (unit-less), which is wider than the average width 0.13 when $\alpha = 1.8$.

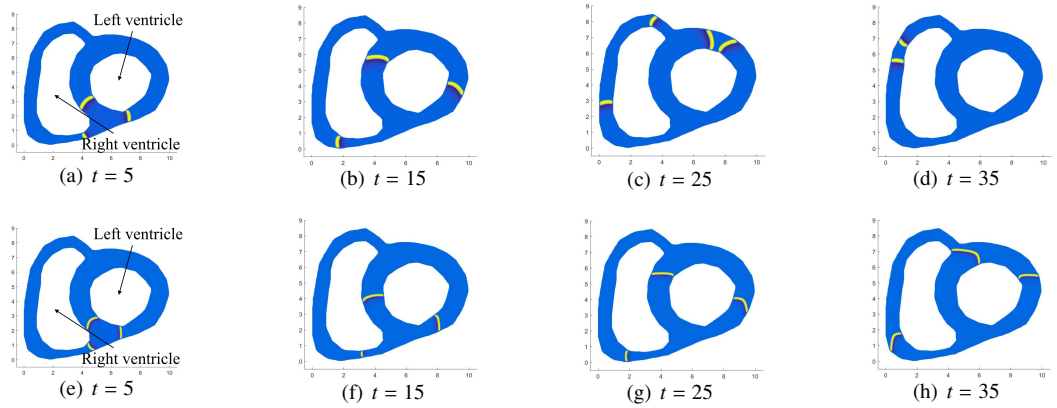

(a) $t = 5$ (b) $t = 15$ (c) $t = 25$ (d) $t = 35$

(e) $t = 5$ (f) $t = 15$ (g) $t = 25$ (h) $t = 35$

Fig. 7. Test 4: The computed solutions of the fractional FHN monodomain model in the transverse section of the ventricle at different time points: (a)-(d) $\alpha = \beta = 2$; (e)-(h) $\alpha = \beta = 1.8$.

It is expected that when two transmembrane potentials meet during propagation, they will stop propagating. Fig. 8 shows the location where the transmembrane potential stops propagating in the left and right ventricles. As seen in Fig. 8, when $\alpha = \beta = 2$, the locations where the transmembrane potentials disappear in the left and right ventricle are the points $(7.80, 7.24)$ and $(0.51, 6.26)$, respectively. When $\alpha = \beta = 1.8$, the stopping points are $(7.82, 7.27)$ (the left ventricle) and $(0.47, 6.17)$ (the right ventricle). This indicates that although the propagation velocity of the transmembrane potential and the width of the wave are gradually decreasing as α decreases, the location at which the transmembrane potential stops propagating essentially does not change.

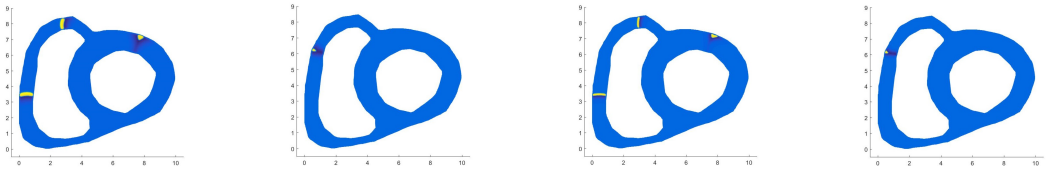

(a) $t = 27.25$ (b) $t = 37.50$ (c) $t = 47$ (d) $t = 65.75$

Fig. 8. Test 4: The locations in left and right ventricles where the transmembrane potential disappears: (a)-(b) $\alpha = \beta = 2$; (c)-(d) $\alpha = \beta = 1.8$.

In order to simulate arrhythmia, an external stimulation is applied in the middle of the interventricular septum at time $t = 10$. The location of the external stimulation is chosen as

$$\widetilde{I}_{\text{sti}}(\mathbf{X}, 10) = \begin{cases} 1, & (X_{10} - 4)^2 + (Y_{10} - 3.5)^2 < (0.5)^2;\ (X_{10}, Y_{10}) \in \Omega_s(10), \\ 0, & \text{otherwise.} \end{cases} \tag{27}$$

Fig. 9 shows the propagation of the transmembrane potential after applying the external stimulation I_{sti}. Figs. 9(a)–9(d) show the simulation results for $\alpha = \beta = 2$. It is clear that the applied external stimulation falls behind the potential wave. Figs. 9(b)–9(d) show that a stable spiral wave is formed in the middle of the interventricular septum. Under the influence of the spiral wave, the transmembrane potential continues to propagate from the middle of the interventricular septum. Figs. 9(e)–9(h) show the propagation of the transmembrane potential after the external stimulation is applied for $\alpha = \beta = 1.8$. It can be seen from Fig. 9(e) that the applied external stimulation just passes through the potential wave in the middle of the interventricular septum. Figs. 9(f)–9(h) show that the applied external stimulation forms two potential waves that propagate in the upper and lower directions in the middle of the interventricular septum, respectively. Similarly, the transmembrane potential propagates cyclically in the heart under the influence of external stimulation. For $\alpha = 1.8$ and $\alpha = 2.0$, the CPU time running up to $t = 40$ are $1975.87s$ and $3523.25s$, respectively.

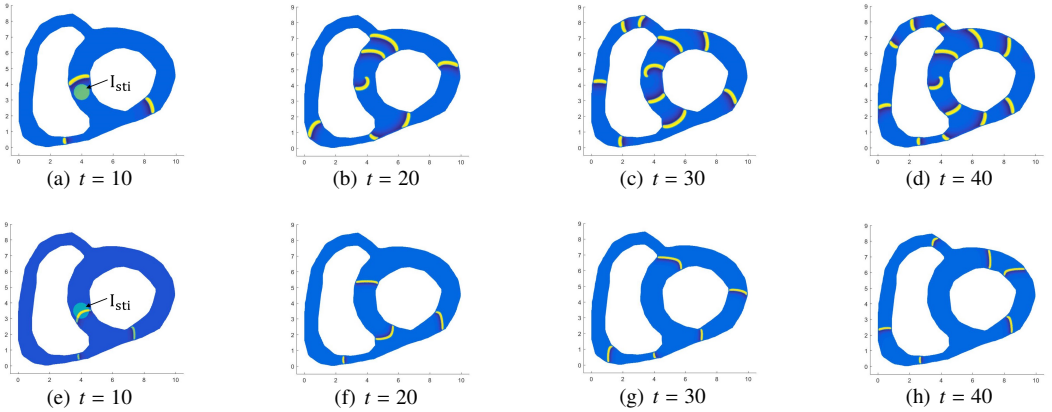

(a) $t = 10$ (b) $t = 20$ (c) $t = 30$ (d) $t = 40$

(e) $t = 10$ (f) $t = 20$ (g) $t = 30$ (h) $t = 40$

Fig. 9. Test 4: The simulation results of the fractional FHN model with the external stimulation: (a)-(d) show the results with $\alpha = \beta = 2$; (e)-(h) show the results with $\alpha = \beta = 1.8$.

Test 5. The same fractional FHN monodomain model as in **Test 3** is considered in this test to study the potential propagation in the two-dimensional moving longitudinal section of the ventricle $\Omega_s(t)$, as shown in Fig. 10(a) with

both the left and right ventricles. Fig. 10 gives the nuclear magnetic resonance (NMR) of a healthy volunteer (cf. [33]). We employ a improved variational level set method (cf. [47]) to segment the ventricle walls from NMR images. The myocardium starts to actively contract after diastole. Under the influence of active contraction, the heart can pump the blood into the systemic circulation (called the pumping process). In this test, the moving boundary effect must be taken into account. The longitudinal section $\Omega_s(t)$ is placed into the ghost structure region $D = [-3.45, 7.05]\times[1.55, 10.45]$. The goal is to simulate the propagation of transmembrane potential during the pumping process. The homogeneous Neumann boundary condition is again imposed on $\Gamma_{\Omega_s}(t)$, and the following simple homogeneous initial conditions are used

$$\widetilde{u}(\mathbf{X}, 0) = 0 \qquad \text{in } \Omega_s(0),$$
$$\widetilde{v}(\mathbf{X}, 0) = 0 \qquad \text{in } \Omega_s(0).$$

In this test, the spatial mesh sizes are chosen as $\Delta x = \Delta y = 0.025$ and the time step size as $\Delta t = 0.2\Delta x$, which implies that the computational domain D is partitioned into 420×356 grids.

At $t = 0$, a constant electrical stimulation ($\widetilde{I}_{\text{sti}} = 1$) is applied to the mid-lower part of the endocardium of the heart (cf. [48, 8]), as shown in the blue region in Fig. 10(a). Under the influence of external electrical stimulation, the transmembrane potential spreads from the endocardium to the entire heart. The left and right ventricles in the longitudinal section will contract inward during the whole simulation time. In order to complete the simulation, we need to determine the location of each Lagrange point during the pumping process. Fig. 10(b)- 10(f) give the NMR images of the heart at different time steps, which describe the movement of the heart. Based on the NMR images, we use the Demon algorithm (cf. [49]) to track the movement and to determine the locations of the Lagrange points of the ventricular wall in each NMR image. The area of the longitudinal section of the ventricle changes from 20.10 (unit-less) at $t = 0$ to 23.85 (unit-less) at $t = 11.25$. Based on the locations obtained by Demon algorithm, we use the linear interpolation to obtain the locations of the Lagrangian points at different time steps.

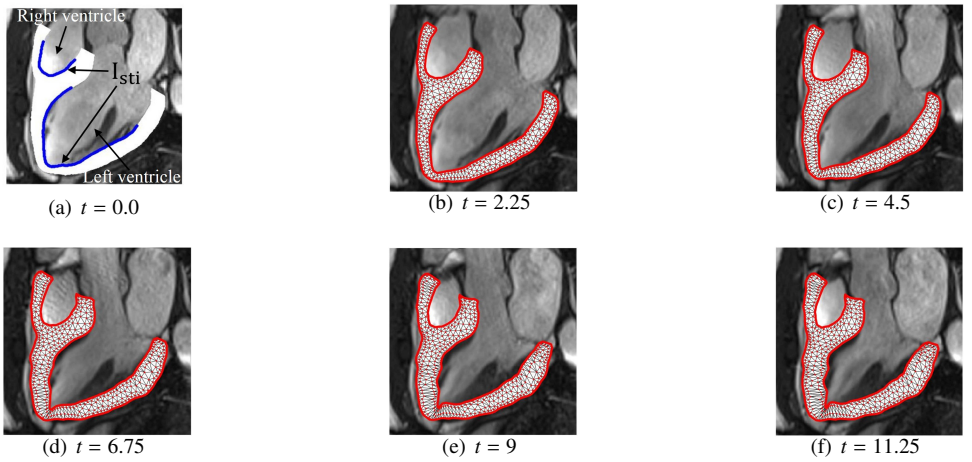

(a) $t = 0.0$ (b) $t = 2.25$ (c) $t = 4.5$

(d) $t = 6.75$ (e) $t = 9$ (f) $t = 11.25$

Fig. 10. Test 5: (a) shows the sketch of I_{sti} in the longitudinal section of the ventricle; (b)-(f) show locations of Lagrangian points at different times obtained by the Demon algorithm.

Fig. 11 shows the transmembrane potential propagation during the pumping process. Figs. 11(a)–11(d) show the propagation of the transmembrane potential when $\alpha = \beta = 2$, Figs. 11(e)–11(h) and Figs. 11(i)–11(l) show the propagation when $\alpha = \beta = 1.8$ and $\alpha = \beta = 1.6$, respectively. When $\alpha = \beta = 2$, the propagation time of the transmembrane potential is about 9.75 (unit-less), which is less than the required time 10.5 when $\alpha = \beta = 1.8$ and 10.75 when $\alpha = \beta = 1.6$. Moreover, when $\alpha = \beta = 2$, the average wave width of the transmembrane potential wave is 0.29 (unit-less), which is wider than the average wave width 0.23 when $\alpha = \beta = 1.8$ and 0.21 when $\alpha = \beta = 1.6$. Thus, the propagation velocity and the wave width of the membrane potential wave decrease with the decrease of α. For $\alpha = 1.6$, $\alpha = 1.8$ and $\alpha = 2.0$, the CPU time running up to $t = 9$ are 10677.2s, 10679.1s and 11083.5s, respectively.

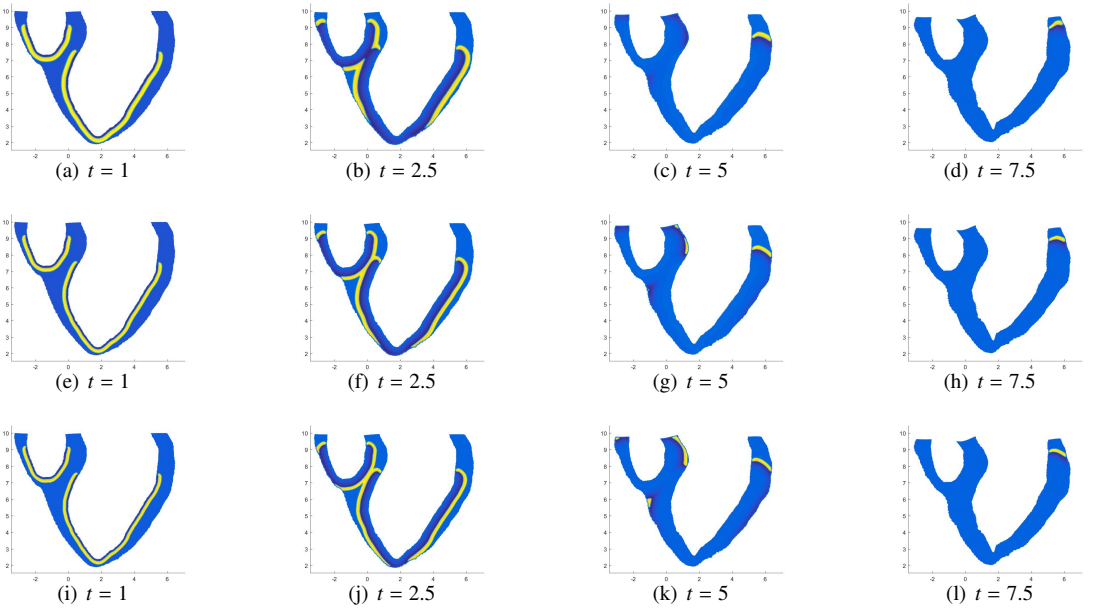

Fig. 11. Test 5: The simulation results of the fractional FHN monodomain model in the longitudinal section of the ventricle during the pumping process: (a)-(d) $\alpha = \beta = 2$**; (e)-(h)** $\alpha = \beta = 1.8$**; (i)-(l)** $\alpha = \beta = 1.6$**.**

6. Conclusion

In this paper, we developed a ghost structure (GS) finite difference method for solving the fractional FitzHugh-Nagumo (FHN) monodomain model on a moving irregular computational domain, which allows efficient discretizations of domain-dependent fractional derivatives appeared in the model. The effectiveness and robustness of the proposed method are verified by a number of numerical tests. In order to analyze the transmembrane potential propagation in both healthy hearts and hearts with arrhythmia, we employed the proposed method to simulate the fractional FHN monodomain model in a transverse section of a heart. We also studied the potential propagation during the pumping process by using the proposed method to simulate the fractional FHN model in the moving longitudinal sections of this heart. The numerical results show that the changes of the fractional derivatives affect the propagation velocity of the transmembrane potential and the width of the potential wave. At the same time, the numerical results demonstrate that the proposed GS finite difference method can efficiently solve the fractional FHN monodomain model in a complexly deformed structure.

In order to analyze the errors and the convergence orders of method, we used our GS finite difference method to solve the two-dimensional Riesz fractional reaction-diffusion equation. The numerical results show that spatial and temporal convergence orders are close to 2 and 1, respectively. We were able to capture the patterns of heterogeneity and complex connectivity of electrophysiological dynamics in biological tissues by solving the fractional FHN monodomain model in the circular region. The spiral wave obtained by our GS finite difference method is qualitatively the same as those obtained by the existing methods. We observed that as the fractional orders α and β decrease, the wave width of the spiral wave decreases gradually. Compared to the isotropic case, the shape of the spiral wave changes significantly in the anisotropic case, from circular to elliptical. Despite of solving the problem in an enlarged computational domain and converting values between the Eulerian and Lagrangian variables, the CPU time required by the proposed GS finite difference method is comparable to existing methods. By simulating the fractional FHN model in a rectangular region with four holes with an external stimulation in the central region of the structure, we analyzed the potential propagation in arrhythmia. For $\alpha = \beta = 2$, under the influence of the external stimulation, we observed that the potential begins to propagate cyclically in the structure and the velocity of transmembrane potential decreases as α and β decrease.

We further simulated the FHN monodomain model in the stationary transverse and moving longitudinal sections of the ventricle. When no external stimulation was applied, we found that the propagation velocity and the width of the transmembrane potential wave decrease with the decrease of α and β. However, the spatial derivatives do not affect

the location where the transmembrane potential disappears. In order to analyze the potential propagation in a heart with arrhythmia, we applied an external stimulation in the transverse section of the heart. Due to the slowdown of the propagation, the applied external stimulation has different effects on potential propagation. For $\alpha = \beta = 2$, the external stimulation falls behind the potential wave. Under the influence of the potential and external stimulus, a stable spiral wave is formed in the middle of the interventricular septum. As the spiral wave propagates outward, the potential begins to propagate cyclically in the heart. For $\alpha = \beta = 1.8$, the applied external stimulation just passes through the potential wave and forms two potential waves that propagate in the upper and lower directions in the middle of the interventricular septum, respectively. Due to the influence of the downward propagating potential, the potential begins to propagate cyclically in the heart. Thus, in a heart with arrhythmia, the transmembrane potential begins spontaneously and repeatedly to immerse into the region where the excitation occurs, and stimulate cardiomyocytes to contract again, which explain why arrhythmia leads to unsynchronized active contraction frequency. To analyze the transmembrane potential propagation during the pumping process, we simulated the fractional FHN monodomain model in the moving longitudinal section of the ventricle. The numerical results again show that the propagation velocity and the width of the potential wave gradually decrease with the decrease of α and β. The numerical results also demonstrate that our GS finite difference method can effectively solve the fraction FHN monodomain model in a deformed structure.

Declaration of competing interest

The authors declare that they have no known competing financial interests or personal relationships that could have appeared to influence the work reported in this paper.

Acknowledgment

Y. H. Wang and L. Cai were supported by the National Natural Science Foundation of China Grants (#11871399 and #11471261). X. Y. Luo and H. Gao were supported by the UK EPSRC (EP/N014642/1) and (EP/S030875/1).

References

[1] C. W. Taber, D. Venes, Taber's cyclopedic medical dictionary, F. A. Davis Company, 2009.
[2] R. Mehra, Global public health problem of sudden cardiac death., Journal of Electrocardiology 40 (2007) 118–122.
[3] D. P. Nickerson, P. J. Hunter, Cardiac cellular electrophysiological modeling, Cardiac Electrophysiology Methods & Models (2010) 135–158.
[4] S. M. Shuaiby, M. A. Hassan, A. B. Sharkawy, A finite element model for the electrical activity in human cardiac tissues., J. Ecol. Heal. Environ 1 (2013) 25–33.
[5] F. B. Sachse, Computational Cardiology, Springer Berlin Heidelberg, 2004.
[6] R. Fitzhugh, Impulses and physiological states in theoretical models of nerve membrane, Biophysical Journal 1 (1961) 445–466.
[7] L. Cai, Y. Sun, F. F. Jing, Y. Q. Li, X. Q. Shen, Y. F. Nie, A fully discrtet implicit-explicit finite element method for solving the fitzhugh-nagumo model, Journal of Computational Mathematics (2019).
[8] Y. Wang, L. Cai, X. Luo, W. Ying, H. Gao, simulation of action potential propagation based on the ghost structure method, Scientific reports 9 (2019) 10927.
[9] R. Metzler, J. Klafter, The random walks guide to anomalous diffusion: a fractional dynamics approach. phys rep, Physics Reports 339 (2000).
[10] R. Metzler, J. Klafter, The restaurant at the end of the random walk: Recent developments in the description of anomalous transport by fractional dynamics, Journal of Physics A General Physics 3737 (2004).
[11] A. Bueno-Orovio, D. Kay, V. Grau, B. Rodriguez, K. Burrage, Fractional diffusion models of cardiac electrical propagation: role of structural heterogeneity in dispersion of repolarization, Journal of the Royal Society Interface 11 (2014).
[12] R. H. Clayton, O. Bernus, E. M. Cherry, H. Dierckx, F. H. Fenton, L. Mirabella, A. V. Panfilov, F. B. Sachse, G. Seemann, H. Zhang, Models of cardiac tissue electrophysiology: Progress, challenges and open questions, Progress in Biophysics and Molecular Biology 104 (2011) 22–48.
[13] L. B. Feng, P. Zhuang, F. Liu, I. Turner, Y. T. Gu, Finite element method for space-time fractional diffusion equation, Numerical Algorithms 72 (2016) 749–767.
[14] Z. Yang, Z. Yuan, Y. Nie, J. Wang, X. Zhu, F. Liu, Finite element method for nonlinear riesz space fractional diffusion equations on irregular domains, Journal of Computational Physics 330 (2017) 863–883.
[15] F. Liu, P. Zhuang, I. Turner, K. Burrage, V. Anh, A new fractional finite volume method for solving the fractional diffusion equation, Applied Mathematical Modelling 38 (2014) 3871–3878.
[16] L. Cai, M. Guo, Y. Li, W. Ying, H. Gao, X. Luo, Nonstandard finite difference method for nonlinear riesz space fractional reaction-diffusion equation., International Journal of Numerical Analysis & Modeling 16 (2019).
[17] B. B. Mandelbrot, The fractal geometry of nature, volume 173, WH freeman New York, 1983.
[18] R. Gorenflo, F. Mainardi, Random walk models for space-fractional diffusion processes, Lecture Notes in Physics (1998) 148–166.

[19] A. D. Freed, K. Diethelm, Fractional calculus in biomechanics: a 3d viscoelastic model using regularized fractional derivative kernels with application to the human calcaneal fat pad, Biomechanics and modeling in mechanobiology 5 (2006) 203–215.

[20] A. Dokoumetzidis, R. Magin, P. Macheras, A commentary on fractionalization of multi-compartmental models, Journal of pharmacokinetics and pharmacodynamics 37 (2010) 203–207.

[21] A. Bueno-Orovio, D. Kay, K. Burrage, Fourier spectral methods for fractional-in-space reaction-diffusion equations, Bit Numerical Mathematics 54 (2014) 937–954.

[22] J. Bai, X. Feng, Fractional-order anisotropic diffusion for image denoising, IEEE transactions on image processing 16 (2007) 2492–2502.

[23] F. Liu, M. M. Meerschaert, R. J. McGough, P. Zhuang, Q. Liu, Numerical methods for solving the multi-term time-fractional;wave-diffusion equation, Fractional Calculus & Applied Analysis 16 (2013) 9–25.

[24] Z. Wang, S. Vong, Compact difference schemes for the modified anomalous fractional sub-diffusion equation and the fractional diffusion-wave equation, Journal of Computational Physics 277 (2014) 1–15.

[25] K. Burrage, N. Hale, D. Kay, An efficient implicit fem scheme for fractional-in-space reaction-diffusion equations, SIAM Journal on Scientific Computing 34 (2012) 2145–2172.

[26] Y. Liu, Y. Du, H. Li, J. Wang, An h^1-galerkin mixed finite element method for time fractional reaction–diffusion equation, Journal of Applied Mathematics and Computing 47 (2015) 103–117.

[27] F. Zeng, F. Liu, C. Li, K. Burrage, I. Turner, V. Anh, A crank–nicolson adi spectral method for a two-dimensional riesz space fractional nonlinear reaction-diffusion equation, SIAM Journal on Numerical Analysis 52 (2014) 2599–2622.

[28] Q. Yang, I. Turner, T. Moroney, F. Liu, A finite volume scheme with preconditioned lanczos method for two-dimensional space-fractional reaction-diffusion equations, Applied Mathematical Modelling 38 (2014) 3755–3762.

[29] Y. Jiang, J. Ma, High-order finite element methods for time-fractional partial differential equations, Journal of Computational & Applied Mathematics 235 (2011) 3285–3290.

[30] J. C. Ren, Z. Z. Sun, Numerical algorithm with high spatial accuracy for the fractional diffusion-wave equation with neumann boundary conditions, Journal of Scientific Computing 56 (2013) 381–408.

[31] B. E. Griffith, X. Y. Luo, Hybrid finite difference/finite element immersed boundary method, International Journal for Numerical Methods in Biomedical Engineering 33 (2017).

[32] L. Cai, H. Gao, X. Y. Luo, Y. F. Nie, Multi-scale modelling of the human left ventricle, Scientia Sinica Physica, Mechanica and Astronomica 45 (2015).

[33] L. Cai, Y. H. Wang, H. Gao, Y. Q. Li, X. Y. Luo, A mathematical model for active contraction in healthy and failing myocytes and left ventricles, Plos One 12 (2017).

[34] F. Liu, I. Turner, V. Anh, Q. Yang, K. Burrage, A numerical method for the fractional fitzhughnagumo monodomain model, Anziam Journal 53 (2013) 608–629.

[35] F. Liu, P. Zhuang, I. Turner, V. Anh, K. Burrage, A semi-alternating direction method for a 2-d fractional fitzhughnagumo monodomain model on an approximate irregular domain, Journal of Computational Physics 293 (2015) 252–263.

[36] G. Jiang, D. Peng, Weighted eno schemes for hamilton-jacobi equations, Siam Journal on Scientific Computing 21 (1997) 2126–2143.

[37] C. W. Shu, S. Osher, Efficient implementation of essentially non-oscillatory shock-capturing schemes, Journal of Computational Physics 77 (1988) 439–471.

[38] C. W. Shu, High Order Weighted Essentially Nonoscillatory Schemes for Convection Dominated Problems, Society for Industrial and Applied Mathematics, 2009.

[39] C. Celik, M. Duman, Crank-nicolson method for the fractional diffusion equation with the riesz fractional derivative, Journal of Computational Physics 231 (2012) 1743–1750.

[40] V. V. Der, Bi-cgstab: A fast and smoothly converging variant of bi-cg for the solution of nonsymmetric linear systems, Siam Journal on Scientific & Statistical Computing 13 (1992) 631–644.

[41] Z. Gong, Research on the Immersed Boundary Method and Its Application on Cell Mechanics, Ph.D. thesis, Shanghai Jiao Tong University, 2010.

[42] J. M. Stockie, Analysis and computation of immersed boundaries, with application to pulp fibres, The University of British Columbia (Canada), 1997.

[43] C. S. Peskin, The immersed boundary method, Acta Numerica (2002) 479–517.

[44] S. Balay, J. Brown, K. Buschelman, V. Eijkhout, W. Gropp, Petsc users manual revision 3.3, Sports Medicine 23 (2013) 21–30.

[45] W. Ying, A multilevel adaptive approach for computational cardiology, Duke University, 2005.

[46] N. Cusimano, L. Gerardo-Giorda, A space-fractional monodomain model for cardiac electrophysiology combining anisotropy and heterogeneity on realistic geometries, Journal of Computational Physics 362 (2018) S0021999118301165.

[47] L. Cai, H. Gao, W. Xie, Variational level set method for left ventricle segmentation, in: Tencon IEEE Region 10 Conference, 2013, pp. 1–4.

[48] N. David, S. Nicolas, H. Peter, New developments in a strongly coupled cardiac electromechanical model, Europace 7 Suppl 2 (2005) 118–127.

[49] H. Lombaert, L. Grady, X. Pennec, N. Ayache, F. Cheriet, Spectral log-demons: Diffeomorphic image registration with very large deformations, International Journal of Computer Vision 107 (2014) 254–271.